Peer-reviewed version available at *Materials* **2018**, *11*, 2026; doi:10.3390/ma11102026

Article

Estimation of the Onset of Crack Growth in Ductile Materials

Andrzej Neimitz [1*], Jaroslaw Galkiewicz[2], Sebastian Lipiec [3] and Ihor Dzioba [4]

[1] Kielce University of Technology; neimitz@tu.kielce.pl
[2] Kielce University of Technology; jgalka@tu.kielce.pl
[3] Kielce University of Technology; slipiec@tu.kielce.pl
[4] Kielce University of Technology; pkmid@tu.kielce.pl

* Correspondence: neimitz@tu.kielce.pl; Tel.: +48-604-918-131

Abstract: In this paper, the ductile fracture mechanism is discussed. The results of the numerical and experimental analyses are used to estimate of the onset of the crack front growth . It is assumed that the ductile fracture in front of the crack starts at the location along the crack front where the accumulated effective plastic strain reaches a critical value. It is also assumed that the critical effective plastic strain depends on the stress triaxiality and the Lode angle. The experimental programme was performed using five different specimen geometries, three different materials and three different temperatures of +20°C, -20°C and -50°C. Using the experimental data and the results of the finite element computations, the critical effective plastic strains are determined for each material and each temperature. However, before the critical effective plastic strain is determined, a careful calibration of the stress–strain curves was performed after modification of the Bai–Wierzbicki procedure. Finally, by analysing the experimental results recorded during the interrupted fracture tests and scanning microscopy observations, the research hypothesis is verified.

Keywords: ductile fracture, ductile fracture mechanisms, critical effective plastic strain, stress triaxiality, Lode angle.

1. Introduction

The failure of ferritic steels covers a wide spectrum of fracture mechanisms that depend on both micro-structure and temperature. At room temperature or at temperatures that are not too low, ductile fracture dominates. However, although the ductile fracture mechanism in most cases is a result of voids nucleation, growth and coalescence, different images of fracture surfaces can be observed. Different images are a result of different levels of the stress triaxialities and Lode angles (factors). When the stress triaxiality is high, the dimples are deep, and the coalescence mechanism is caused by necking of inter-void ligaments (Fig. 1a). When the stress triaxiality is low, the dimples are shallow and elongated, suggesting significant shear plastic strains and shear localization between voids (Fig. 1b,)..Also a ductile failure may take place as a result of a dislocation's glide along the slip planes (Fig. 1c).

Here, the stress triaxiality is measured using the η parameter:

$$\eta = \frac{\sigma_m}{\sigma_e} \tag{1}$$

where σ_m and σ_e are the first stress tensor invariant and effective stress, respectively; $\sigma_e = \sqrt{3J_2}$, and J_2 is the second stress deviator invariant.

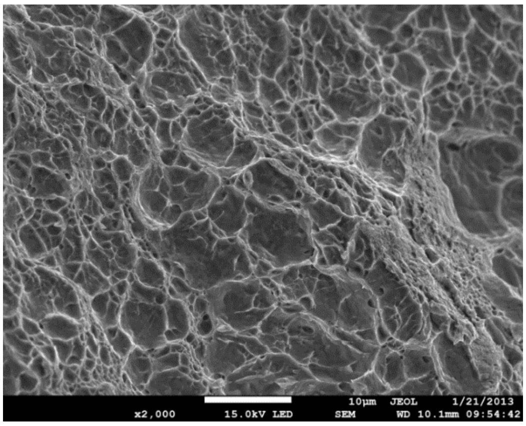

Fig. 1a. Dimples in front of the crack, central part of the specimen

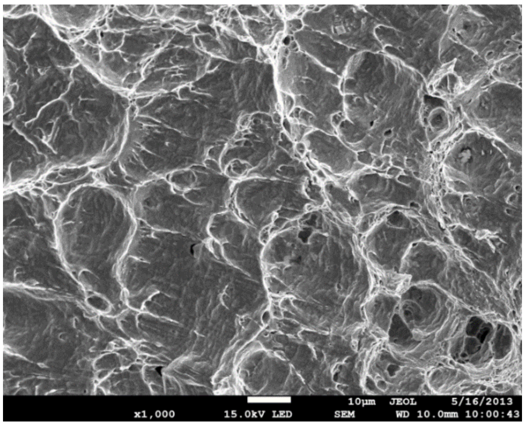

Fig. 1b. Dimples in front of the crack, located at the mid-part of the shear lips

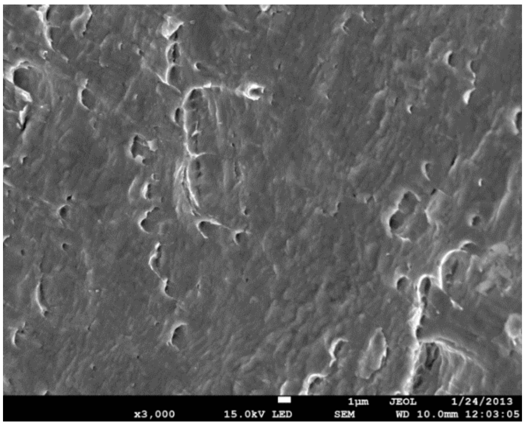

Fig. 1c. The traces of dimples in front of the crack, located close to the specimen surface - shear lips

All these mechanisms of ductile fracture can be observed in front of the crack. However, the stress triaxiality factor alone is not always sufficient to explain the changes in the failure mechanism. It is suggested that other parameters that could be helpful in qualitative and quantitative analysis of fracture mechanisms are the accumulated effective plastic strain and the Lode angle/factor. The Lode angle θ, or one of the Lode parameters ξ, or L are defined as follows:

$$\cos(3\theta) = (r/\sigma_e)^3 = \xi = 27/2 \cdot J_3/\sigma_e^3 \tag{2}$$

where θ $r = \left[27/2 \det(s_{ij})\right]^{1/3} = \left[27/2(\sigma_1 - \sigma_m)(\sigma_2 - \sigma_m)(\sigma_3 - \sigma_m)\right]^{1/3}$, s_{ij} is the stress tensor deviator, and J_3 is the third invariant of the stress deviator. In this paper, the Lode factor is used, the value of which can be computed from the following formula:

$$L = -\frac{2\sigma_{II} - \sigma_I - \sigma_{III}}{\sigma_I - \sigma_{III}} \tag{3}$$

and L is related to the ξ function by the relationship: $\xi = L\left(9-L^2\right)/\sqrt{\left(L^2+3\right)^3}$. In Eq. 3, σ_I is the highest principal stress, and σ_{III} is the smallest principal stress; L=1(or L=-1) when the axial symmetric tensile (or compressive) loading is met; L=0 when pure shear is met in the plane stress state. Other loading cases are located in between the above values.

The exemplary distributions of η, L and the accumulated effective plastic strain, ε_{eff_pl}, along the crack front are shown in Fig. 2.

The curves in Fig. 2 were obtained by the finite element method using the ABAQUS program. The boundary conditions were adopted from the experiment with the single–edge–notch–bend (SEN(B)) specimen. The thickness of the specimen was B=12 mm, and the width was W=24 mm. The half of the specimen thickness was divided into 10 layers.

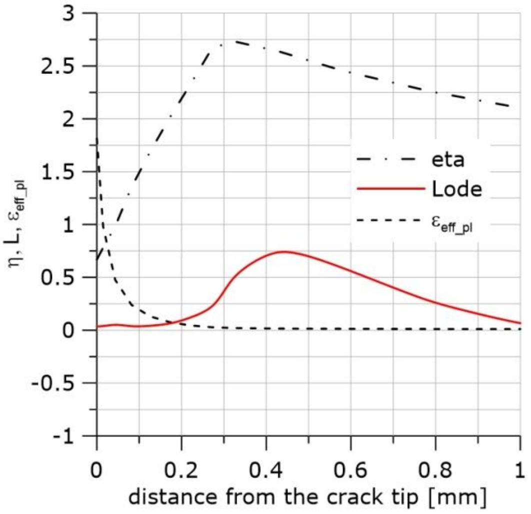

Fig. 2a. Distributions of η, L and ε_{eff_pl} in front of the crack at the central part of the specimen

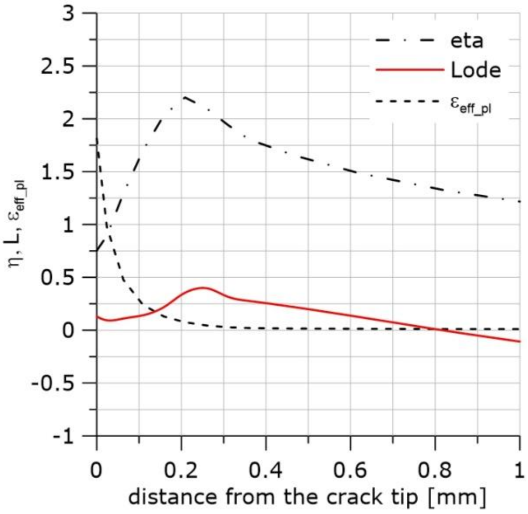

Fig. 2b. Distributions of η, L and ε_{eff_pl} in front of the crack at the layer located 1.75 mm from the surface

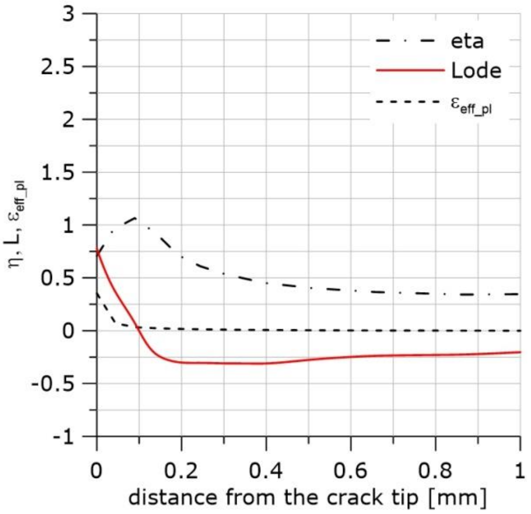

Fig. 2c. Distributions of η, L and ε_{eff_pl} in front of the crack at the next to last layer from the specimen axis

Large strains and J_2 plasticity were assumed. Linear, hexagonal C3D8 elements (ABAQUS) with full integration were used. The crack tip was blunted by a 10 μm radius. The size of the finite elements increased with the distance from the crack tip. The size of the smallest element in the radial direction

doi:10.20944/preprints201809.0511.v1

Peer-reviewed version available at *Materials* **2018**, *11*, 2026; doi:10.3390/ma11102026

was 27 μm. The thickness of the layers through the specimen thickness decreased towards the specimen external surface. The thinnest layer was 0.27 mm.

In contrast to the cleavage fracture, it is very difficult to predict the onset of crack growth in ductile materials. Ductile crack growth due to voids nucleation–growth–coalescence is found to initiate at different moments at different locations along the blunted crack front. This moment is not noticeable when the load-deflection curve is observed, and the onset of a crack growth usually occurs when this curve is still rising. This trait is a reason that standards are proposed to measure the critical value of the J-integral after the presumable 0.2 mm average crack front extension.

The purpose of the research programme reported in this paper was to estimate and predict the moment and location of the onset of the ductile crack extension.

The research hypothesis is that a crack starts growing by the void nucleation–growth–coalescence mechanism when the accumulated effective plastic strain reaches the critical value. Following the results of numerous papers [1–16], it was assumed that the critical effective plastic strain depends on the triaxiality parameter and the Lode angle/factor.

In Section 2, the mechanical properties of three materials measured at three temperatures are presented, and five specimen shapes used in the research program are shown. The shapes of the specimens were selected to generate different combinations of stress triaxialites and Lode angles. In Section 3, the calibration of the stress–strain curves is presented. The calibration was performed with the modified Bai-Wierzbicki procedure [4]. The modification included evolution of the stress triaxiality and Lode factors as well as the material softening due to the void growth and coalescence. In Section 4, the critical effective plastic strains are determined. In Section 5, the results of the numerical computations of the mechanical field's parameters in front of the crack are shown. The effect of the stress-strain calibration on the stress distribution is presented. Finally, in Section 6, the results of the interrupted fracture tests (SEN(B) specimens) are shown and compared with the evolution of the effective plastic strains in front of the crack. The verification of the research hypothesis is demonstrated.

2. Materials and tested specimens

The calibration of the constitutive equations and determination of the critical values of the accumulated effective plastic strains was performed using the specimens shown in Fig. 3.

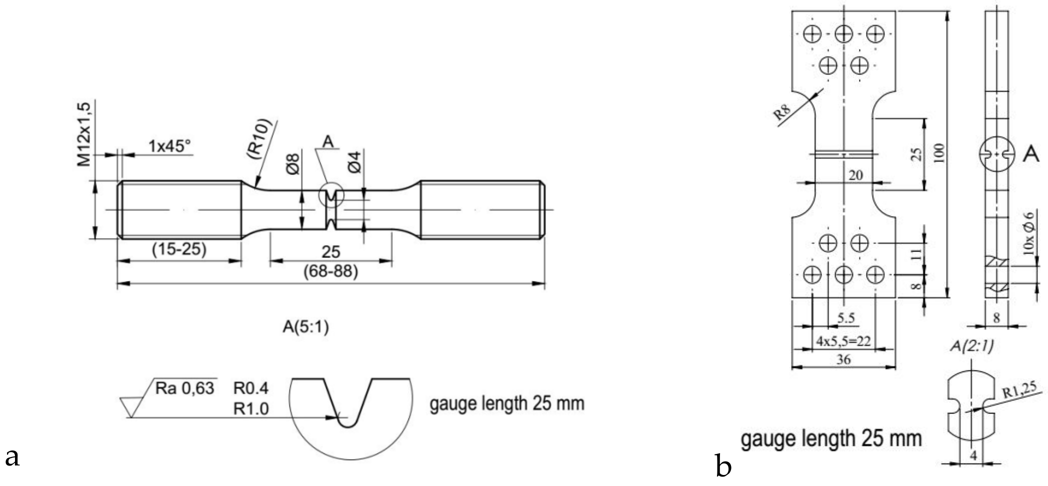

Peer-reviewed version available at *Materials* **2018**, *11*, 2026; doi:10.3390/ma11102026

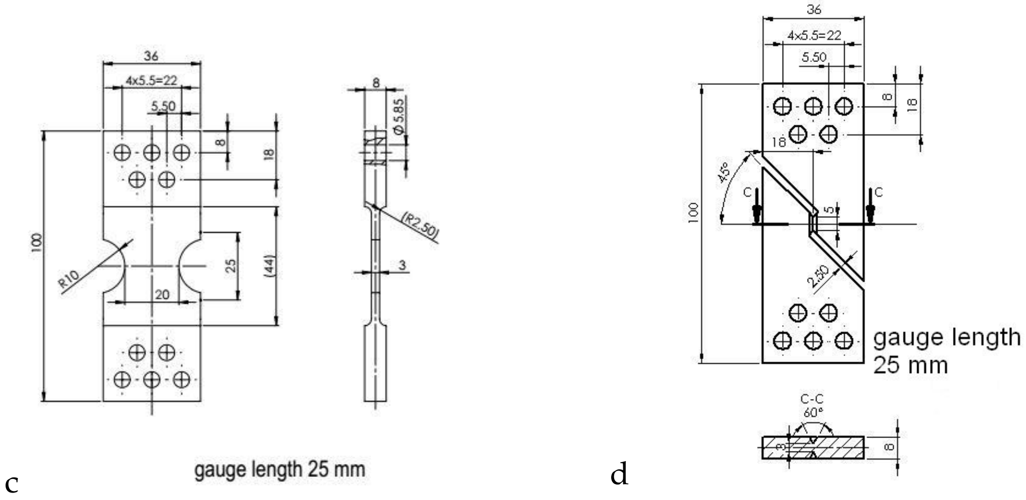

Fig. 3. Tested geometries: a) two notched cylindrical specimens C04 with R=0.4 mm ($\eta\approx$ from 0.5 to 1.6; L≈ from 0.6 to 1) and C1 with R=1 mm ($\eta\approx$ from 0.4 to 1.4; L≈ from 0.85 to 1); b) plate with side groove (PN), R=1 mm ($\eta\approx$ 0.4; L=0.4); c) plate with R=10 mm (PR) ($\eta\approx$ 0.5; L=0.5) and d) pure shear (S) ($\eta\approx$ 0; L=0)

The mechanical properties of the materials tested in the research programmes are listed in Table 1. Different temperature levels were used to control the extent of plasticity.

Table 1. The mechanical properties of the materials tested in the research programmes

	Heat Treatment	Microstructure	Temp. °C	*E* [GPa]	R_{eL} [MPa]	R_{eH} [MPa]	R_m [MPa]
S355JR steel, symbol NW	Normalized and annealed (600°C, 150 h)	Ferrite containing spheroidized carbide particles	+20 -20 -50	210 200 212	382 376 390	368 419 396	470 502 526
S355JR steel, symbol HW	Quenching in oil and annealed (600°C, 150 h)	Ferrite containing spheroidized carbide particles	+20 -20 -50	197 191 210	412 437 463	406 444 488	511 555 581
S355JR steel, symbol N	Normalized at 950°C	Ferrite–pearlite	+20 -20 -50	197 202 220	367 402 401	375 407 428	496 526 553

3. Calibration of the constitutive relationships

To perform the finite element analysis on any shape and size of the machine or structural member the uniaxial stress–strain curves, are required. It turns out that the results of standard uniaxial tensile tests alone are not sufficient, especially when the large plastic strains are expected. It is not sufficient to only convert stresses to the true stresses and strains to the logarithmic strains. The stress triaxiality and the way a specimen is loaded should also be taken into account to ensure conformity between numerical and experimental results. Thus, the stress–strain curves must be calibrated before they are used by the finite element code. In research papers, when both the experimental and numerical results are used to prove some hypotheses, the problem of the stress–strain relationship is not often discussed. The calibration of the tensile test curves is either not performed or it is a result of the curve fitting by the trial and error method; however, sometimes it is performed by a well-defined methodology, e.g., [3], [4], [11]. In this research programme, we adopt the Bai–Wierzbicki (BW) methodology [3], which involves both the stress triaxiality factor η and the

Lode parameter. Eq. 4 is selected from the several equivalent formulae proposed by BW and other authors:

$$\sigma_{yld} = \bar{\sigma}\left(\bar{\varepsilon}_p\right)\left[1 - c_\eta\left(\eta - \eta_0\right)\right]\left[c_\theta^s + \left(c_\theta^{ax} - c_\theta^s\right)\left(\gamma - \frac{\gamma^{m+1}}{m+1}\right)\right] \tag{4}$$

where η_0 is a reference value of the triaxiality coefficient; and η_0=1/3 for the uniaxial tensile test. The γ function represents a curve drawn at the deviatoric surface between the contours defined by the Huber–von Mises and Tresca criteria in the principal stress space. The γ function satisfies the inequality $0 \le \gamma \le 1$, where γ=0 for plane stress or pure shear, and γ=1 for axial symmetry. BW postulated that the γ function takes the following form:

$$\gamma = \frac{\cos(\pi/6)}{1-\cos(\pi/6)}\left[\frac{1}{\cos(\theta - \pi/6)} - 1\right] = 6.464\left[\sec(\theta - \pi/6) - 1\right] \tag{5}$$

In Eq. 4, the quantity c_θ^{ax} is defined as follows:

$$c_\theta^{ax} = \begin{matrix} c_\theta^t & for & \bar{\theta} \ge 0 \\ c_\theta^c & for & \bar{\theta} < 0 \end{matrix} \tag{6}$$

$\bar{\theta} = 1 - 6\theta/\pi$. Eq. 4 contains four parameters to be determined: c_θ^t, c_θ^c, c_θ^s and m. The term containing the m parameter is added to make the yield surface smooth and differentiable with respect to the Lode angle θ in the neighbourhood of γ=1. These parameters must be determined experimentally; however, at least one of them is equal to unity. If $\bar{\sigma}\left(\bar{\varepsilon}_p\right)$ is found through a uniaxial tensile test using cylindrical specimens, then $c_\theta^t = 1$. If a uniaxial compression test is performed, then $c_\theta^c = 1$, and in the case of a shear test, $c_\theta^s = 1$. In the original BW methodology, both η and θ parameters are assumed constant during the specimen loading. Here, it is assumed that both η and L parameters change over the critical plane and over time during the loading process. The average values of these quantities over the critical plane are introduced into Eq. 4. The η function changes according to Eq. 7.

$$\eta = \eta_i - \left(\frac{\eta_i - \eta_f}{\varepsilon_{pl\_avr\_final}}\right)\varepsilon_{pl\_avr} \tag{7}$$

where index i denotes the initial state, index f denotes the final state, $\varepsilon_{pl\_avr\_final}$ is the average value of the effective plastic strain in the critical plane before the failure and ε_{pl_avr} is the actual average effective plastic strain in the critical plane. A similar formula was used for the Lode parameter. The average values over the critical plane are assumed because the force–elongation curve represents the average response of the specimen to the external loading.

Comparison of the experimental and numerical results during the calibration process leads to the conclusion that the softening of the material during the loading process caused by the void growth and coalescence at the final stage of loading should also be taken into account. Thus, it is assumed that c_η in Eq.4 takes the form:

$$c_\eta = \alpha\left[1 + H\left(\varepsilon_{eff\_pl} - \varepsilon_{eff\_pl\_o}\right)\left(\varepsilon_{eff\_pl} - \varepsilon_{eff\_pl\_o}\right)\right]^\zeta \tag{8}$$

where $\varepsilon_{eff\_pl\_o}$ denotes the value of the effective plastic strain at the presumed onset of rapid void growth. $H(\varepsilon_{eff\_pl} - \varepsilon_{eff\_pl\_o})$ is the Heaviside step function; coefficients α and ζ should be determined experimentally.

More details concerning the calibration of the stress–strain curves according to the procedure described above can be found in [17].

In Fig. 4, the exemplary curves determined experimentally and numerically after and before calibration are presented. The examples cover the whole temperature range and three specimens.

Peer-reviewed version available at Materials 2018, 11, 2026; doi:10.3390/ma11102026

Before calibration, each stress–strain curve is converted to the true stress – logarithmic strain (TS-LS) curve, and after the maximum is reached, it is extrapolated either as a power function or linear function. An approximation of the TS-LS curve by a power function leads to good results for a plastic material at room temperature. When the test temperature is lowered, such an approximation is not always recommended because, in many cases, using the power function may lead to a situation where the calibration procedure proposed in this paper cannot be applied; see Fig. 4d.

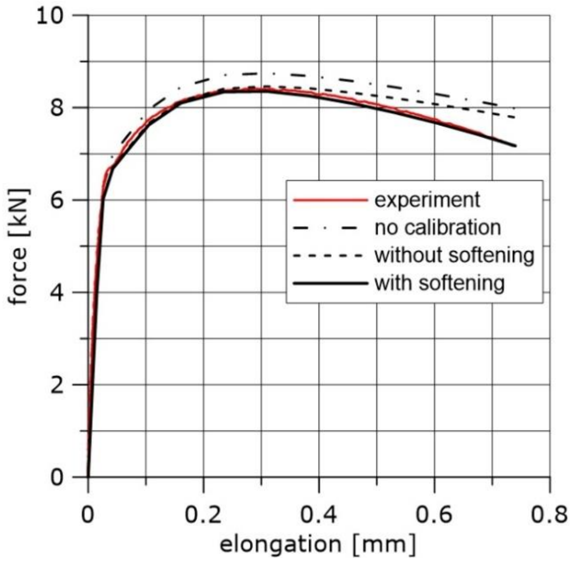

Fig. 4a. Calibrated true stress–logarithmic strain curves; material NW, specimen for calibration: R1, temp. +20°C

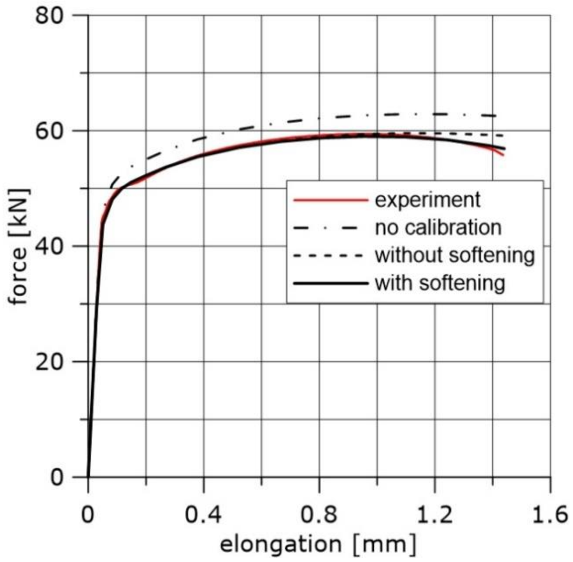

Fig. 4b. Calibrated true stress-logarithmic strain curves; material HW, specimen for calibration: PN, temp. -20°C

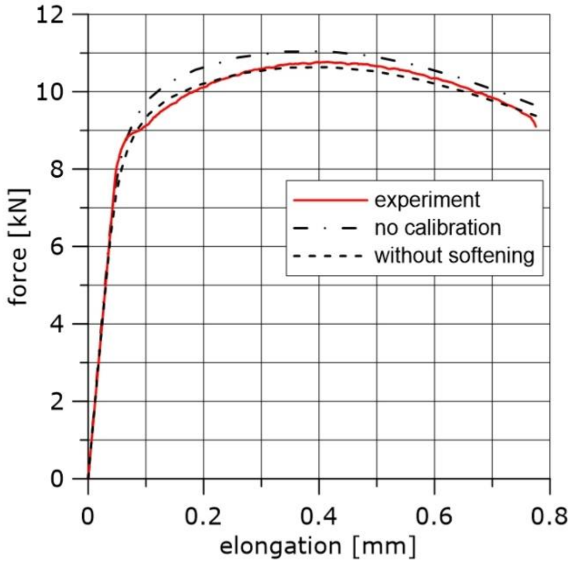

Fig. 4c. Calibrated true stress–logarithmic strain curves; material N, specimen for calibration: R04, temp. -50°C, linear approximation

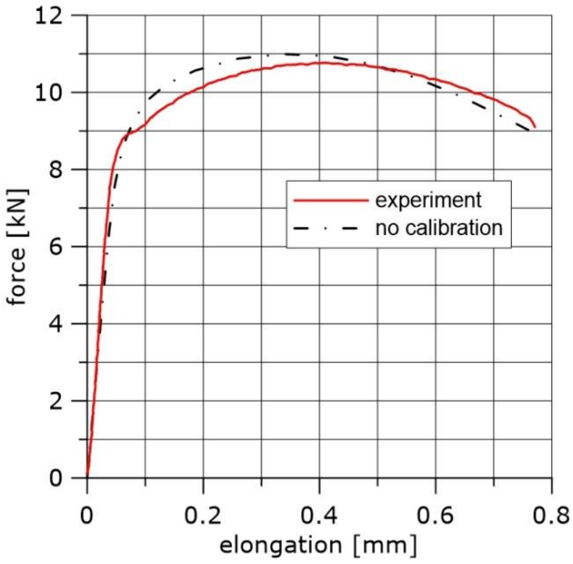

Fig. 4d. Calibrated true stress–logarithmic strain curves; material N, specimen for calibration: R04, temp. -50°C, power function approximation

4. Critical accumulated effective plastic strain

According to several research reports, beginning with studies by McCintock [18] and Rice and Tracey [19], the critical strain at the onset of ductile failure depends (at least) on stress triaxiality, measured, e.g., by the η parameter. Recently, it was noticed [1], [2] that the critical strain also depends on the Lode angle or Lode parameter defined in Section 1. The Lode angle describes how the specimen or structural member is loaded.

The specimens used for the TS-LS curves calibration were also used for estimation of the critical effective plastic strains for all three materials and three temperatures.

After specimen failure, the fracture surfaces of broken specimens were observed using the electron scanning microscope, and finite element analyses were performed using the ABAQUS program. During numerical computations, the finite elements from the ABAQUS standard library were used. In the case of specimens C04 and C1, 4–node, reduced–integration, axisymmetric, solid elements were used (symbol CAX4R). Because large gradients of the computed quantities were not expected, the size of the element next to the notch was 0.138 mm. The other two cases (PN and PR specimens) were modelled using linear 3D hexagonal elements with the reduced integration (C3D8R). The sizes of the element in the direction of the greatest stress gradient were 1/20 width of the specimen, that is, 1.0 mm for the PR specimen and 0.086 mm for the PN specimen. In the case of the S specimen, the C3D8R elements were used, and the size of the element in the shear region was 0.2 mm. The symmetries of the modelled specimens were taken into account to reduce the time of computations. The specimens were loaded by displacements applied at the distance determined by the gauge length (see Fig. 3). As a result of numerical computations, the following quantities were recorded over the critical plane: η, L, $\varepsilon_{eff\_pl\_cr}$, and σ_{22}, where σ_{22} is the crack faces opening stress. The microscopic observations revealed, in most cases, the ductile failure via the void mechanism (Fig. 5a and 5b), in some cases, failure due to the slip over slip planes (Fig. 5c) took place (in this case, the L parameter must be close to zero), and, in some cases, the cleavage failure mechanism (Fig. 5d) was observed. The later mechanism was observed at low temperatures.

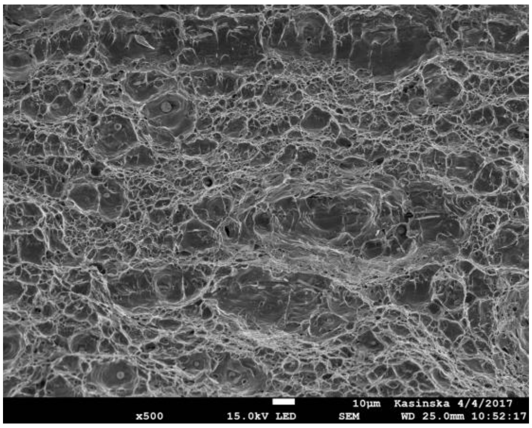

Fig. 5a. Dimples along the fracture surface in specimen C1; material N, temp. +20°C

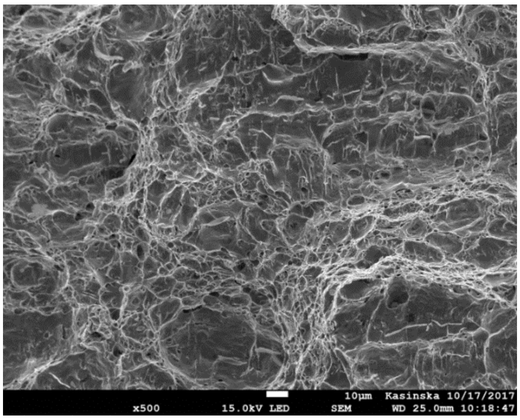

Fig. 5b. Dimples along the fracture surface in specimen PN; material N, temp. +20°C

Peer-reviewed version available at *Materials* **2018**, *11*, 2026; doi:10.3390/ma11102026

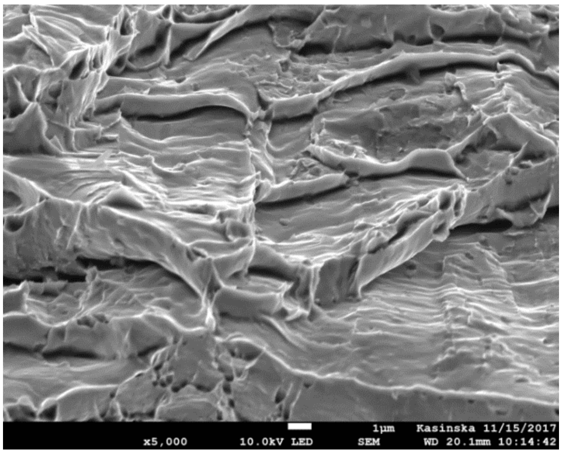

Fig. 5c. Ductile fracture due to the dislocations glides along the slip planes; specimen PR; material HW, temp. -20°C

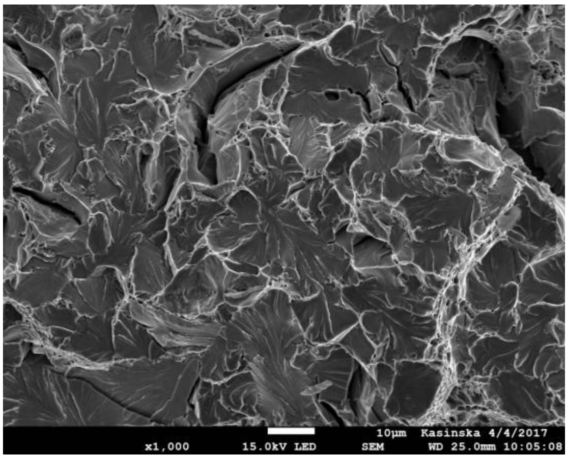

Fig. 5d. Cleavage fracture next to the circumferential notch in specimen C04; material NW, temp. -50°C

The microscopic observations alone are not sufficient to decide, in most cases, at which part of the critical plane the final stage of the void growth–coalescence process initiated. It was assumed that, at such a place, the dimples must be the largest. In the most cases, both within cylindrical and PN specimens, the differences between the sizes and shapes of caverns were not clearly noticeable. Thus, a working hypothesis had to be assumed to localize the critical spot. The origin of this hypothesis is Rice and Tracy's [19] results concerning the rate of growth of the isolated spherical void surrounded by an ideally plastic material. Their numerical results were well approximated by the formula: $\frac{\dot{R}_0}{R_0} \cong 0.263\dot{\varepsilon}\exp\left(\frac{\sigma_m}{2\sigma_e}\right)$. Because the whole critical cross-section of the loaded specimen is stretched at the same time, it is proposed to compare the quantity representing, in a very rough approximation, the extension of the voids' radii, recorded along the fractured surface at the presumed moment of the rapid evolution of damage. The simplified formula is as follows:

$$V = \Delta R = \Delta\varepsilon_{eff\_pl}\exp(\eta) \tag{9}$$

The exemplary results concerning two cylindrical specimens with different radii at the bottom of the circumferential notch are shown in Fig. 6 and Table 2.

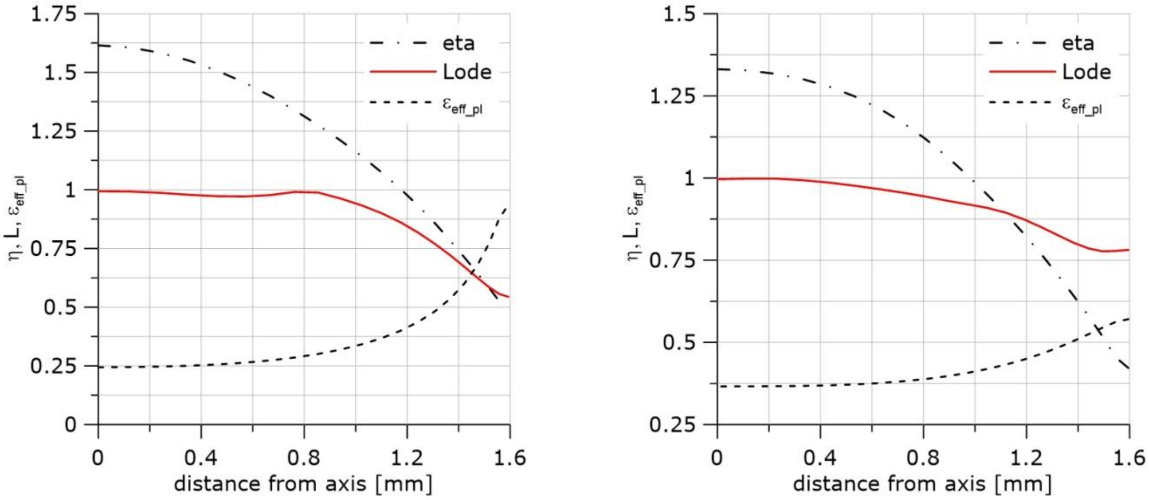

Peer-reviewed version available at *Materials* **2018**, *11*, 2026; doi:10.3390/ma11102026

Fig. 6a. Distribution of η, L, ε_{eff_pl}; specimen C04, material HW, temp. +20°C, last step of the integration

Fig. 6b. Distribution of η, L, ε_{eff_pl}; specimen C1, material HW, temp. +20°C, last step of the integration

Table 2. Values of the mechanical field parameters at the critical moment along the fracture surface for C04 and C1 specimens, material HW, temperature +20°C.

		$\varepsilon_{eff\_pl\_cr}$	η	L	σ_{max}	$\varepsilon_{eff\_pl\_cr} \cdot \exp(\eta)$
R=0.4	**Specimen centre**	0.24	1.6	0.99	1443	1.19
	Next to the notch	0.93	0.497	0.54	789	**1.53**
R=1.0	**Specimen centre**	0.36	1.33	0.996	1298	**1.36**
	Next to the notch	0.57	0.42	0.78	619	0.86

It was concluded from the results listed in Table 2 that the final ductile failure process initiated at the centre of the C1 specimen and next to the notch in the C04 specimen. Similar results are shown for the PN specimen. In this case, the critical spot is either close to the specimen longer axis at the specimen centre or next to the notch at the specimen central part (see Table 3).

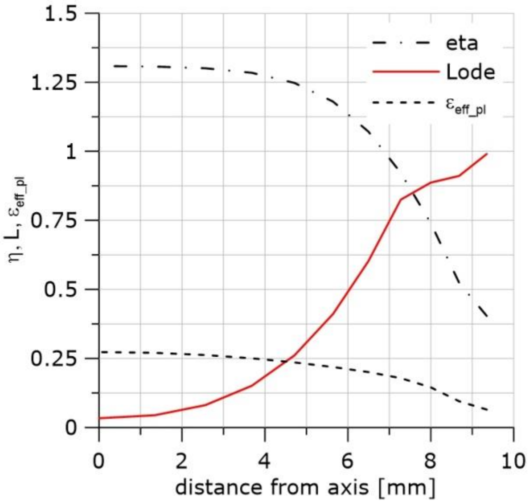

Fig. 7a. Distribution of η, L, ε_{eff_pl} along longer specimen axis; specimen PN, material HW, temp. +20°C, last step of the integration

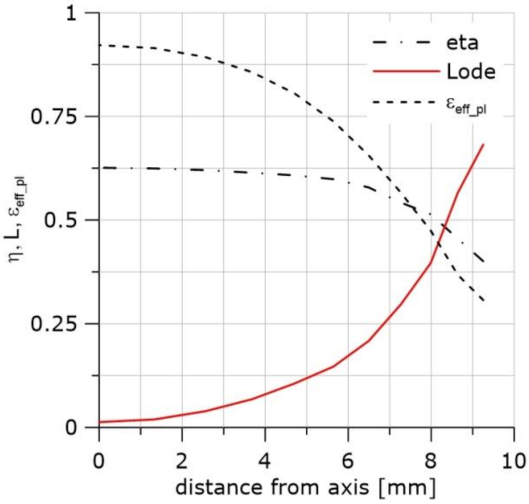

Fig. 7b. Distribution of η, L, ε_{eff_pl} along notch; specimen PN, material HW, temp. +20°C, last step of the integration

Peer-reviewed version available at Materials 2018, 11, 2026; doi:10.3390/ma11102026

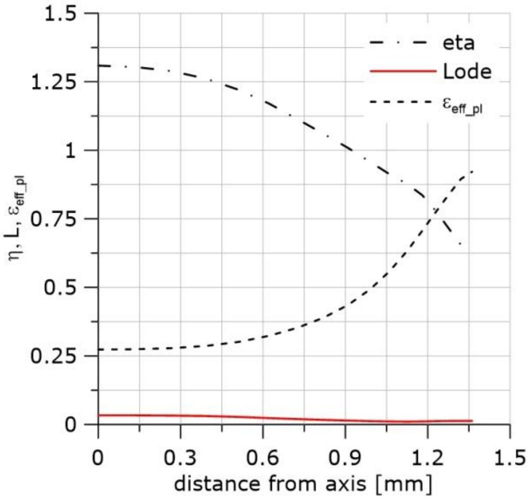

Fig. 7c. Distribution of η, L, ε_{eff_pl} along shorter specimen axis; specimen PN, material HW, temp. +20°C, last step of the integration

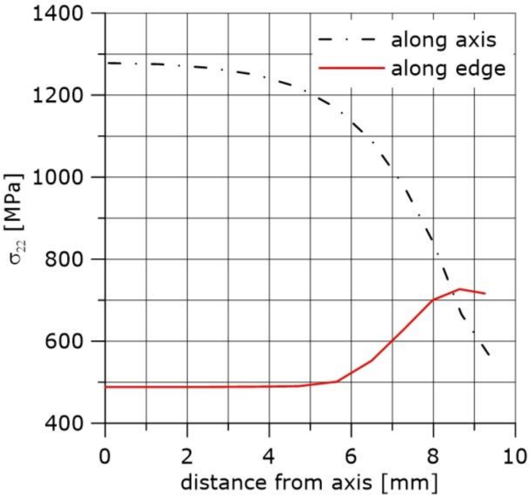

Fig. 7d. Maximum opening stress along the longer stress distribution and along the notch; specimen PN, material HW, temp. +20°C, last step of the integration

Table 3. Values of the mechanical field parameters at the critical moment along the PN specimen fracture surface. Material N. Temperature +20°C

		$\varepsilon_{eff\_pl\_cr}$	η	L	σ_{max}	$\varepsilon_{eff\_pl\_cr} \cdot \exp(\eta)$
PN specimen	Central part next to the axis	0.27	1.3	0.033	1278	0.99
	Central part next to the notch	0.92	0.626	0.013	477	**1.16**

As a result of the observations and computations, each of the critical accumulated effective plastic strains is estimated as a function of the η and L parameters. Using these values and the least square method, the surfaces of the critical strains are estimated in the η, L, $\varepsilon_{eff\_pl\_cr}$, space for all three materials and temperatures. The equation used in the least square method is as follows:

$$\varepsilon_{eff\_pl\_cr} = \omega \exp(\beta\eta) + (a\eta + b)L^2 + c\eta + d \qquad (10)$$

Parameters ω and β are determined as the coefficients of the exponential function in Eq. 10. This function approximates all experimental points for three materials tested, three temperatures and five specimen geometries. The experimental points and the trend line are shown in Fig. 8. The two parameters are ω=1.88 and β=-1.25.

Peer-reviewed version available at Materials 2018, 11, 2026; doi:10.3390/ma11102026

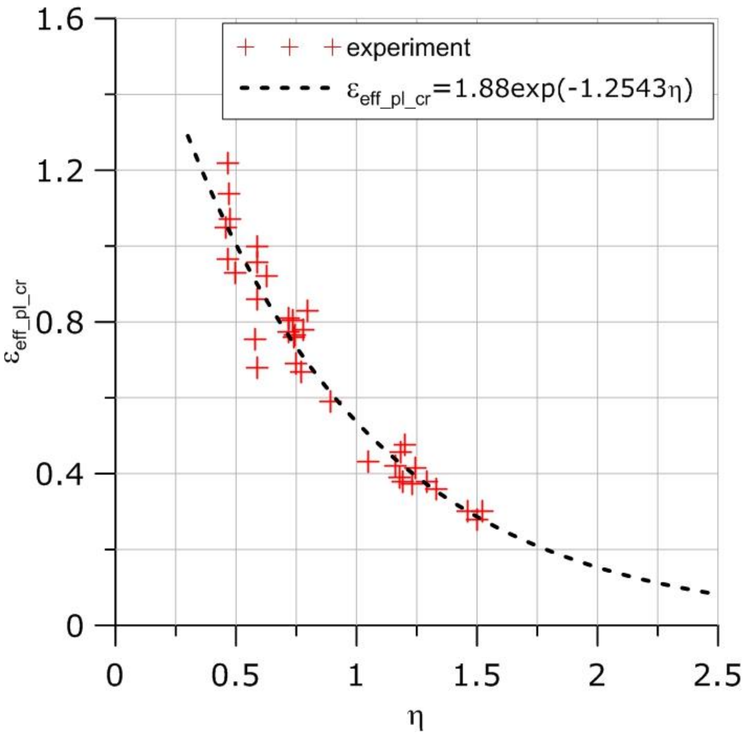

Fig. 8. Exponential dependence between the critical strain and the triaxiality factor

In Table 4, all parameters other than ω and β in Eq. 11 are shown.

Table 4. Parameters entering Eq. 10 for the three materials and three temperatures tested.

material	**HW**	**HW**	**HW**	**N**	**N**	**N**	**NW**	**NW**	**NW**
temp	**-20**	**-50**	**20**	**-20**	**-50**	**20**	**-20**	**-50**	**20**
a	-0.065	-0.016	-0.099	-0.038	-0.01	-0.07	-0.04	-0.030	-0.12
b	0.121	0.036	0.25	0.113	0.018	0.23	0.11	0.097	0.33
c	-0.046	-0.02	-0.118	-0.07	-0.026	-0.07	-0.087	-0.01	-0.015
d	0.135	0.032	0.227	0.14	0.064	0.126	0.21	0.0024	-0.0027

The exemplary surfaces for materials N and HW and temperature +20°C are shown in Fig. 9. To draw these surfaces, the values of the coefficients in Eq. 10 are as follows: a=-0.072, b=0.233; c=-0.074; d=0.126 (material N) and a=-0.099, b=0.252; c=-0.118; d=0.227 (material HW).

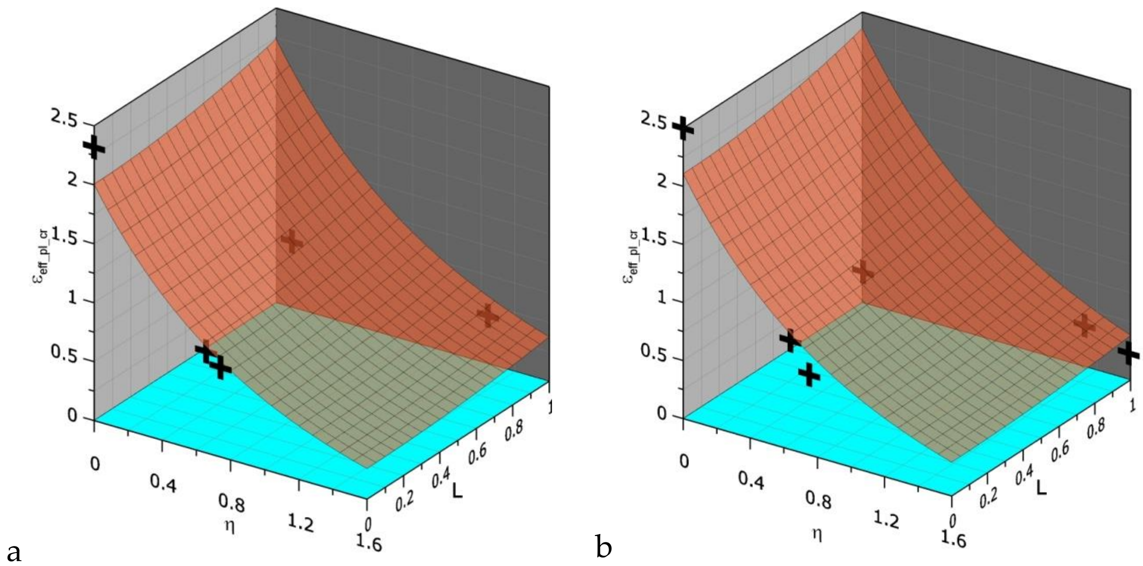

Fig. 9. Three-dimensional dependence between η, L and $\varepsilon_{eff\_pl\_cr}$ for N material (a), and HW material (b)

5. Stress distribution in front of the crack

Stress distributions in front of the crack in the SEN(B) specimen computed numerically depend on the calibration process of the constitutive equations. The exemplary curves are shown in Fig. 10 for uncalibrated stress–strain curves and for various calibration procedures.

The details of the specimen geometry and the finite element computations are shown in Section 1.

Note that the calibration that takes into account material softening at the last stage of loading leads to acceptable results from the physical point of view; the curves go down towards the crack tip after the stress maximum is reached. It is not very important what shape of specimen is used for the calibration, provided the stress triaxiality is high enough. The stress maximum in front of the crack after calibration of the constitutive equation (N material, temp. +20°C) is lower by 2.6% with respect to the results obtained after computation without calibration. The stress maximum is in the range of 1291 to 1297 MPa for the results of computations obtained using calibrated stress–strain curves. Differences between the distances of the stress maximum from the crack tip are within the range of 4 μm. Thus, it turns out that if the region next to the crack front is not of the researcher's interest, the calibration procedure can be ignored.

Peer-reviewed version available at *Materials* **2018**, *11*, 2026; doi:10.3390/ma11102026

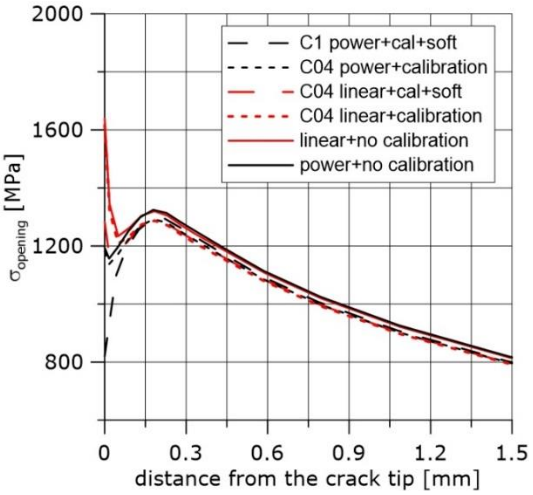

a

b

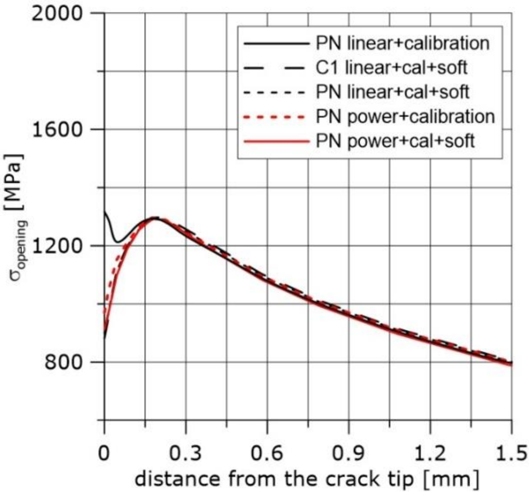

Peer-reviewed version available at *Materials* **2018**, *11*, 2026; doi:10.3390/ma11102026

Fig. 10. Opening stress distribution computed numerically using stress–strain curves after several calibration procedures

6. Accumulated effective plastic strain distributions in front of the crack

In Fig. 11a, selected exemplary curves (5 of 16) of the strain distributions in front of the crack are presented. The difference between the values of the effective plastic strain at the blunted crack tip obtained after computations using uncalibrated stress–strain curves and calibrated curves including the process of material softening is 15%. In Figs 11b–11d, the effective plastic strain distributions are presented for all layers through the specimen thickness for three selected steps of integration. These curves may be used together with the results presented in Fig. 9 (Eq. 10 and Table 4) to estimate the onset and location of the ductile failure mechanism in front of the crack. The first example concerns the SEN(B) specimen made of the N steel tested at +20°C.

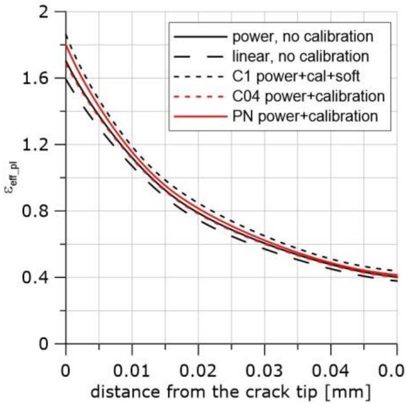

Fig. 11a. Distributions of the effective plastic strain along the crack front at the final moment of loading after calibration using specimen R1 and the material softening option; material N, temp.+20°C

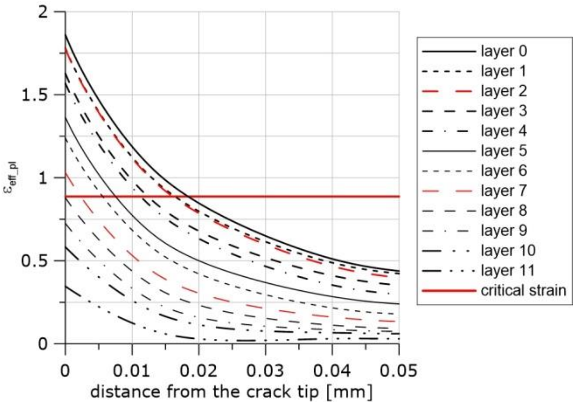

Fig. 11b. Distributions of the effective plastic strain along the front of the crack at the final moment of loading after calibration using specimen R1 and the material softening option; material N, temp.+20°C

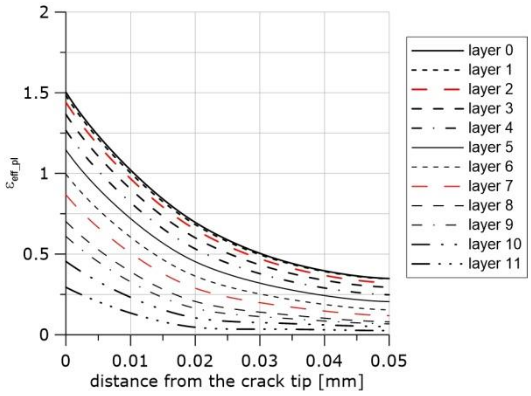

Fig. 11c. Distributions of the effective plastic strain along the front of the crack at the 25th/30th step of loading after calibration using specimen R1 and the material softening option; material N, temp.+20°C

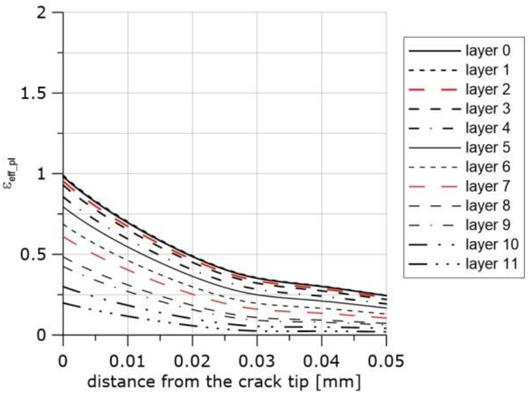

Fig. 11d. Distributions of the effective plastic strain along the front of the crack at the 20th/30th step of loading after calibration using R1 specimen and the material softening option; material N, temp.+20°C

Peer-reviewed version available at Materials 2018, 11, 2026; doi:10.3390/ma11102026

In Fig. 12 the image of the middle part of the SEN(B) specimen after unloading is shown. After the test was interrupted, the specimen was unloaded and then cut off along the central surface of the specimen in the perpendicular direction to the crack front. Next, the machined surface was polished and etched. The image of the crack tip and the voids enables the assessment of the extension of the crack. The crack extension at this location along the crack front due to the voids nucleation and coalescence of voids is in the range of 170–190 μm. The coefficients are $\eta = 0.67$ and L=0.03. According to Eq. 10, $\varepsilon_{eff\_pl\_cr}$=0.887. The strain distributions along the crack front at the moment of unloading are shown in Fig. 11b. The line denoting the critical strain is also shown. One can easily read from these curves that the crack might grow to a distance of approximately 180 μm, and it is very likely that the crack has also grown until the layer 8 along the crack front is reached. One can also presume that the process of nucleation and growth of voids might have started at the middle part of the specimen in front of the crack at the 20th step of loading (max. number of the loading steps was 30), see Fig. 11d.

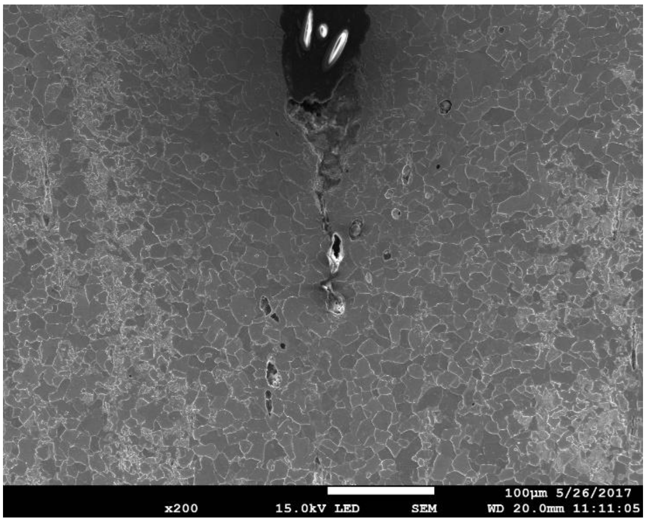

Fig. 12. The image of the surface in front of the crack located at the specimen centre perpendicular to the crack front; material N, temp. +20°C

Another example is shown in Fig. 13. The SEN(B) specimen was made of NW steel and tested at -50°C. When the loading was interrupted, the following values were recorded at the crack tip: η=0.81, L=0.22, and $\varepsilon_{eff\_pl\_cr}$=0.68. In this case, the plastic strain distribution in front of the crack suggests that the crack front might have grown to approximately 160 μm. The microscopic image shows that the crack has grown at this plane by 70-80 μm; however, new voids have already grown in front of the growing crack at the distance of 40-50 μm.

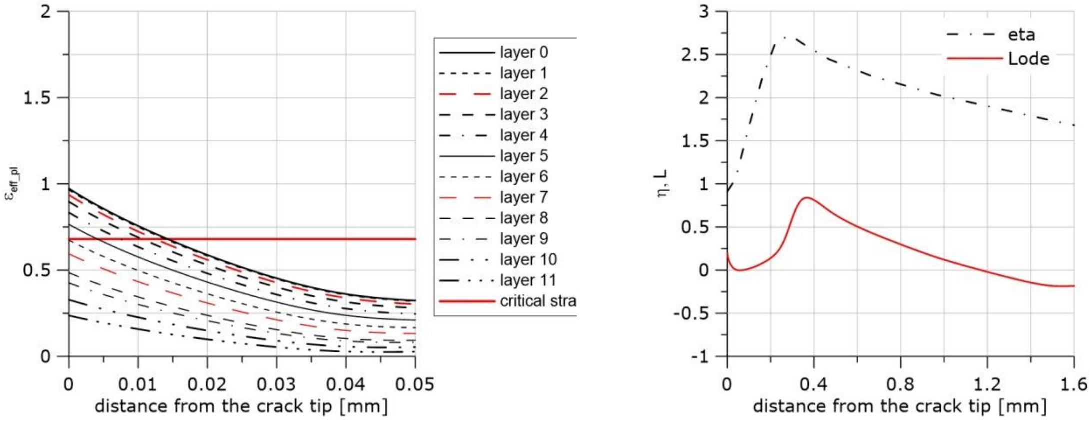

Peer-reviewed version available at *Materials* **2018**, *11*, 2026; doi:10.3390/ma11102026

Fig. 13a**.** Distributions of the effective plastic strain along the crack front at the final moment of loading after calibration using specimen PR and the material softening option; material NW, temp.-50°C

Fig. 13b. Distributions of the η and Lode functions at the crack centre at the moment when the loading was stopped

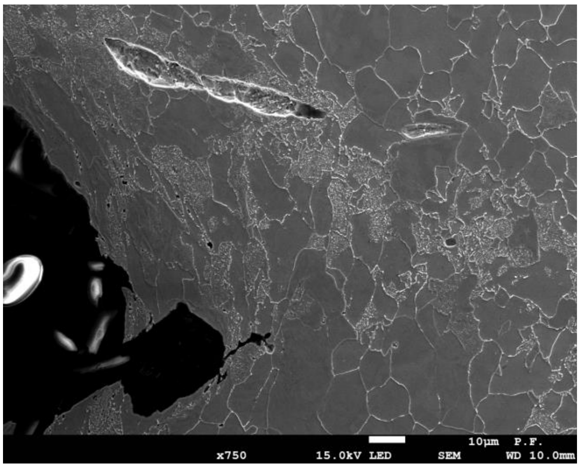

Fig. 13c. The image of the domain in front of the crack at the moment of unloading; the ductile failure mechanism evolves; material NW, temp.-50°C

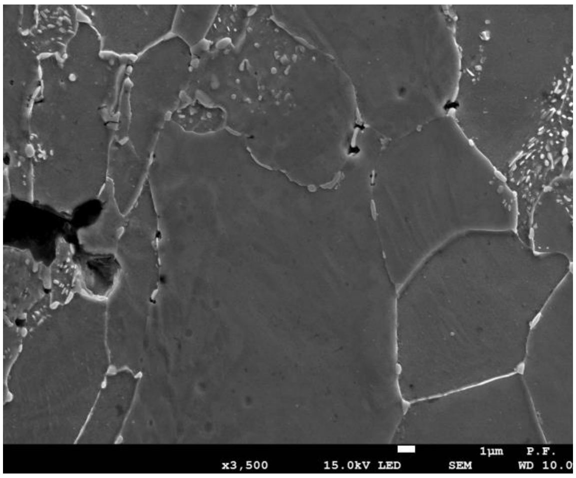

Fig. 13d. The image of the domain in front of the crack at the moment of unloading; the new voids are visible in front of the growing crack

Next example is shown in Fig. 14. The loading of the SEN(B) specimen made of the HW material and tested at +20°C was interrupted before the onset of crack extension. In the image shown in Fig. 14c, one may observe in the fracture surface the trace of a blunted crack front and the individual voids ahead of the blunted crack front. After the specimen unloading, the fatigue loading was applied until the final failure. At the unloading, the following values were recorded at the crack tip: η=0.88, L=0.22, and $\varepsilon_{eff\_pl\_cr}$=0.76 (see Fig. 14b and Eq. 10). The image of the fracture surface and the effective plastic strain distribution in front of the crack at the moment of the specimen unloading indicate that the loading process had been interrupted just before the onset of the crack extension.

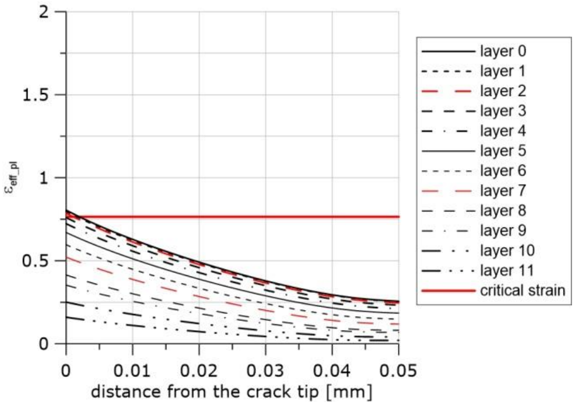

Fig. 14a. Distributions of the effective plastic strain in front of the crack along the crack front at the final moment of loading after calibration using specimen PR and the

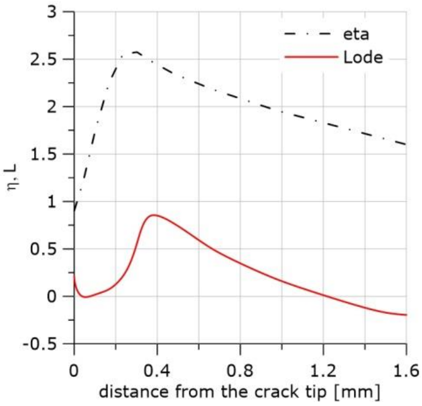

Fig. 14b. Distributions of the η and Lode functions in front of the crack at the crack centre at the moment when the loading was stopped

Peer-reviewed version available at Materials 2018, 11, 2026; doi:10.3390/ma11102026

material softening option; material HW, temp.+20°C

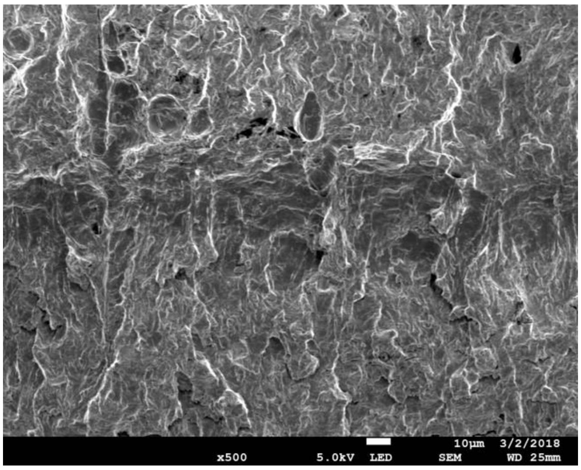

Fig. 14c. The image of the fracture surface obtained using the scanning microscope

7. Summary and conclusions

In this report, selected results of the research programme concerning the analysis of the ductile failure in front of the crack were shown. Three different materials (Table 1) were tested at three different temperatures of +20°C, -20°C and -50°C to control the level of plasticity. The onsets and evolutions of ductile failure in front of the cracks in the SEN(B) specimens were assessed and analysed. It was assumed that a crack starts growing by the voids nucleation–growth–coalescence mechanism when the accumulated effective plastic strain reaches the critical value. In turn, it was assumed after the numerous published papers [1–16] that the critical accumulated effective plastic strain depends on the triaxiality factor and Lode angle. To confirm these assumptions, the experimental programme and numerical computations were performed to a) calibrate the uniaxial tensile curves and b) estimate the critical effective plastic strains. Both tasks were conducted by testing numerous specimens of different five shapes (Fig. 3). The calibration was performed according to the modified BW procedure. The modification included different methods of computing both η and L functions and the softening of material at the last stage of loading via the growth and coalescence of voids. The effect of softening turned out to be the important factor because it caused more physical stress distribution in front of the crack than obtained without softening. The critical effective plastic strains were computed individually for each material and each temperature using the experimental data and the least square statistical method.

Using the distribution of the plastic strains along the crack front and the values of the assessed critical effective plastic strains, the moment and the location of the onset of the ductile crack extension was estimated. The estimations were successfully verified by the scanning microscope observations of the domains in front of the cracks after interrupted tests on the SEN(B) specimens.

Conclusion: The results of the experimental–numerical research programme positively verify the research hypothesis formulated in the Introduction of this paper.

Acknowledgements. This research was performed with financial support from the Polish National Science Committee (NCN), grant no. UMO–2014/15/B/ST8/00205.

8. References

1. Bao, Y., Wierzbicki, T., On fracture locus in the equivalent strain and stress triaxiality space. Int J Mech. Sci. 46(1), (2004), 81–98,

Peer-reviewed version available at *Materials* **2018**, *11*, 2026; doi:10.3390/ma11102026

2. Wierzbicki T., Bao Y., Lee Y-W, Bai Y., Calibration of seven fracture models, International Journal of Mechanical Sciences, 47 (2005), pp. 719-743.
3. Bai, Y., Wierzbicki, T., Application of extended Mohr–Coulomb criterion to ductile fracture, International Journal of Fracture, 161, (2010), pp. 1–20,
4. Bai, Y., Wierzbicki, T., A new model of metal plasticity and fracture with pressure and Lode dependence, International Journal of Plasticity, 24 (2008), pp. 1071–1096,
5. Mohammed Algarni, Yuanli Bai, Youngsik Choi, A study of Inconel 718 dependency on stress triaxiality and Lode angle in plastic deformation and ductile fracture, Engineering Fracture Mechanics 147, (2015), pp. 140–157,
6. Mohr, D., Marcadet, S.J., Micromechanically–motivated phenomenological Hasford–Coulomb model for predicting ductile fracture initiation at low stress triaxialities. International Journal of Solids and structures. 67–68, (2015), pp. 40–45,
7. Bai, Y.,Teng. X, Wierzbicki, T. On the application of stress triaxiality formula for plane strain fracture testing. Journal of Engineering Materials and Technology, 131, (2009).
8. Faleskog J., Barsoum I., Tension-torsion fracture experiments-Part I; Experiments and a procedure to evaluate the equivalent plastic strain, International Journal of Solids and Structures, 50, (2013), pp. 4241-4257.
9. Dunand M., Mohr D., Hybrid experimental-numerical analysis of basic ductile fracture experiments for sheet metals. International Journal of Solids and Structures, 47, (2010), 1130-1143.
10. Dunand M., Mohr D., On predictive capabilities of the shear modified Gurson and the modified Mohr-Coulomb fracture models over a wide range of stress triaxialities and Lode angles. Journal of Mechanics and Physics of Solids, 59, (2011), 1374-1394.
11. Barsoum I., Faleskog J., Pingle S. The Influence of the Lode parameter on ductile failure strain in steel. Science Direct, Procedia Engineering 10, (2011), pp. 69-75.
12. Barsoum I., Faleskog J., Pingle S., The effect of stress state on ductility in moderate stress triaxiality regime of medium and high strength steels. International Journal of Mechanical Sciences, 65, (2012) 203-212.
13. Kofiani K., Nonn A., Wierzbicki T., New calibration method for high and low triaxiality and validation on SENT specimens of API X70. International Journal of Pressure Vessels and Piping, 111-112, (2013) pp. 187-201.
14. Xue L. Damage accumulation and fracture initiation in uncracked ductile solids subject to triaxial loading. International Journal of Solids and Structures, 44, (2007), pp. 5163-5181.
15. Papisidero J., Doquet V., Mohr D., Ductile fracture of aluminium 2024-T351 under proportional and non-proportional multi-axial loading: Bao-Wierzbicki results revisited. International Journal of Solids and Structures, 69-70, (2015), pp. 495-474.
16. Erice B., Galvez F., A coupled elastoplastic-damage constitutive model with Lode angle dependent failure criterion. International Journal of Solids and Structures, 51, (2014), 93-110.
17. Neimitz A., Galkiewicz J., Dzioba I., Calibration of constitutive equations under conditions of large strains and stress triaxiality, Archives of Civil and Mechanical Engineering, Volume 18, Issue 4, September 2018, Pages 1123–1135.
18. McClintock FA. A Criterion for Ductile Fracture by Growth of Holes. Journal of Applied Mechanics 1968; 4:363–371.
19. Rice, J.R., Tracey, D.M., „On the ductile enlargement of voids in triaxial stress fields", Journal of the Mechanics and Physics of Solids, Tom 17, str. 201-217 (1969).